COMMUNICATIONS CHEMISTRY

ARTICLE

https://doi.org/10.1038/s42004-019-0222-4 OPEN

Dynamic covalent chemistry steers synchronizing nanoparticle self-assembly with interfacial polymerization

Fenghua Zhang[1], Zhijie Yang[1,2*], Jinjie Hao[1], Kaixuan Zhao[1], Mingming Hua[1,2], Yanzhao Yang[1*] & Jingjing Wei[1*]

Precise organization of matter across multiple length scales is of particular interest because of its great potential with advanced functions and properties. Here we demonstrate a simple yet versatile strategy that enables the organization of hydrophobic nanoparticles within the covalent organic framework (COF) in an emulsion droplet. The interfacial polymerization takes place upon the addition of Lewis acid in the aqueous phase, which allows the formation of COF after a crystallization process. Meanwhile, the interaction between nanoparticles and COF is realized by the use of amine-aldehyde reactions in the nearest loci of the nanoparticles. Importantly, the competition between the nanoparticle self-assembly and interfacial polymerization allows control over the spatial distribution of nanoparticles within COF. As a general strategy, a wide variety of COF-wrapped nanoparticle assemblies can be synthesized and these hybridized nanomaterials could find applications in optoelectronics, heterogeneous catalysis and energy chemistry.

[1] School of Chemistry and Chemical Engineering, Shandong University, 250100 Jinan, China. [2] Key Laboratory of Colloid and Interface Chemistry, Ministry of Education, Shandong University, 250100 Jinan, China. *email: zyangchem@sdu.edu.cn; yzhyang@sdu.edu.cn; weijingjing@sdu.edu.cn

Supramolecular self-assembly is the process by which the building blocks arrange themselves into an ordered structure, offering a means to control structural features from the sub-nanometer molecular to the nanometer colloidal level[1–5]. The ability to assemble nanoscale building blocks into ordered materials depends crucially on the ability to govern the interparticle interactions[6]. Because self-assembly usually requires that the building blocks equilibrate between the aggregated and non-aggregated states[7], weak noncovalent forces (e.g., van der Waals, hydrogen bonding, hydrophobic, electrostatic) are favored in the formation of self-assembled structures including DNA[8], proteins[9], nanoparticle superlattices[10–12], block copolymer melts[13], and lipid vesicles[14]. In other words, the strong covalent bond is undesirable because the components stick together irreversibly when they collide covalently, forming a glassy aggregate rather than an ordered structure. Nevertheless, recent development of dynamic covalent chemistry enables the cooperative self-assembly of molecular materials and colloidal nanoparticles into hierarchical structures[15].

Covalent organic frameworks (COFs) are a new class of porous polymers constructed by organic molecules with predictable dynamic covalent bonding in two or three dimensions, flexible molecular structures, and high specific surface areas[16–24]. The defined nanoscale channels and pores within COFs represent an ideal environment for molecular storage, release, separation, and catalysis[25–33]. Besides, COFs materials are potentially attractive in electrochemical energy storage and optoelectronic conversion by tethering functional moieties into the organic linkers[34–38]. Another strategy for imparting functionalities into COFs is to hybridize COFs with other functional materials, such as nanoparticles, polymers, and metal-organic frameworks[39–42]. One of the major challenges to integrating COFs with other materials is that COFs are typically formed as insoluble microcrystalline powders, which are difficult to process or not compatible with other materials. Recently, a two-step strategy that enables the encapsulation of nanoparticles into imine-based COF spheres has been reported[43,44]. This relies on the encapsulation of nanoparticles into amorphous imine-based spheres, followed by the crystallization of imine-based polymers under acidic conditions. Another method for integrating COFs with other materials is to use amine functionalized materials that enables the condensation reaction between amine and aldehyde, which ultimately results in the overgrowth of COFs on the amine functionalized materials with a core–shell structure[44].

Although some progress has been made on nanoparticles/COFs hybrids, several significant challenges still need to be addressed. (1) Nanoparticles are protected by a layer of surface-bound molecules (ligands) that endows its colloidal stability. While the surface chemistry of nanoparticles varies from one to another, thus surface modification or surface ligand exchange is indispensable for the compatibility between nanoparticles and COFs. In this regard, a generalized method that enables the intimate contact between nanoparticles and COFs is yet not well developed. (2) An ensemble of colloidal nanoparticles can be allowed to self-assemble into a periodic superlattice, which provides these materials with novel electronic, optical, and catalytic functionalities for nanotechnological applications. Hence the ability to control the position, orientation, and chemical composition of nanoparticles within the COFs is highly desirable and offers a compelling platform to explore high-performance materials. (3) Synthesis of COFs relies on reversible covalent-bond-forming reactions, and it seems that only the reversible reactions are appropriate for the self-assembly of COFs. Meanwhile, self-assembly of nanoparticles involves noncovalent or weak interactions between nanoparticles, and requires that these nanoparticles be mobile[45–48]. Although both synthesis of COFs with periodic structures and self-assembly of nanoparticles into superlattices involve systems that at global or local equilibrium, it remains a significant challenge to correlate the COFs syntheses with nanoparticles' self-assembly.

Here, we report a general approach towards regulating the spatial distribution of colloidal nanoparticles within COFs. This strategy mainly relies on the synchronization of nanoparticle self-assembly with imine bond formation between the organic subunits in a confined medium. We utilize oil-in-water (O/W) emulsion technique for the synthesis of nanoparticles/COFs hybrids. Initially, nanoparticles and the organic subunits for COFs are dissolved in nonpolar solvent. Self-assembly of nanoparticles within the emulsion droplet is triggered by the evaporation of the carrier solvent, whereas the polymerization (imine bond formation) takes place upon the addition of Lewis acid in the aqueous phase. Importantly, the surface of the nanoparticles is capped with oleylamine, which enables the imine bond formation between the oleylamine and the aldehyde in the nearest loci because of the dynamic ligand adsorption/desorption kinetics (Fig. 1). The competition between the self-assembly and polymerization allows control over the spatial distribution of nanoparticles within COFs by adjusting the reaction temperature. The as-prepared nanoparticles/COFs exhibit distinct sensing properties, exemplified by using Au nanoparticles as probes for surface-enhanced Raman spectroscopy (SERS).

Results

Synthesis of colloidal COFs. We utilize O/W emulsion technique for the synthesis of colloidal COFs in a confined space, which requires that the organic subunits are initially dissolved in the oil phase, whereas the catalyst promoting the interfacial polymerization is dissolved in the aqueous phase. In a proof of concept, we choose an imine-linked COF (TAPB-PDA) from 1,3,5-tris(4-aminophenyl)benzene (TAPB) and terephthaldehyde (PDA), which combines the merits of both the solubility of organic subunits and the triggered interfacial polymerization by a Lewis acid, scandium triflates ($Sc(OTf)_3$)[49,50]. In a typical experiment, 1 mL of tetrahydrofuran (THF) containing TAPB and PDA molecules is added to 4 mL of aqueous solution containing of dodecyltrimethylammonium bromide (DTAB) and Sc $(OTf)_3$, followed by emulsification by a vortex. The resulting emulsion is then heated at 70 °C for 30 min to evaporate the inner phase. The resulting colloidal particles can be collected by centrifugation, the scanning electron microscopy (SEM) and transmission electron microscopy (TEM) images reveal that these colloidal particles are spheres with a size of 206.8 ± 30.0 nm in diameter (Fig. 2b–g, Supplementary Fig. 4). Fourier transform infrared (FTIR) spectra confirms the formation of imine bond at 1617 cm^{-1}, which corresponds to the –C = N stretching (Supplementary Fig. 1). We found that this reaction can be probed by the UV–Vis spectroscopy, which relies on the fact that the absorption of the particles at 420 nm increases linearly with the increase of the concentration of particles (Supplementary Fig. 2), following the Beer–Lambert's law. The time-dependent UV–Vis absorption measurements reveal that the polymerization terminates after ~4 min (Supplementary Fig. 3). The rate of the polymerization can be controlled by the temperature. For example, when the temperature is decreased to 30 and 15 °C, respectively, the polymerization process takes 6 and 8 min. Importantly, slowing down the polymerization rate can result in a hollow structure (at 15 °C), which can be clearly identified from the contrast difference between the pale center and the dark edge in the TEM images (Fig. 2h, i). This hollow structure is also proved by the SEM image (Fig. 2j, k). We believe that these hollow spheres are derived from the emulsion droplet templates.[51,52] The

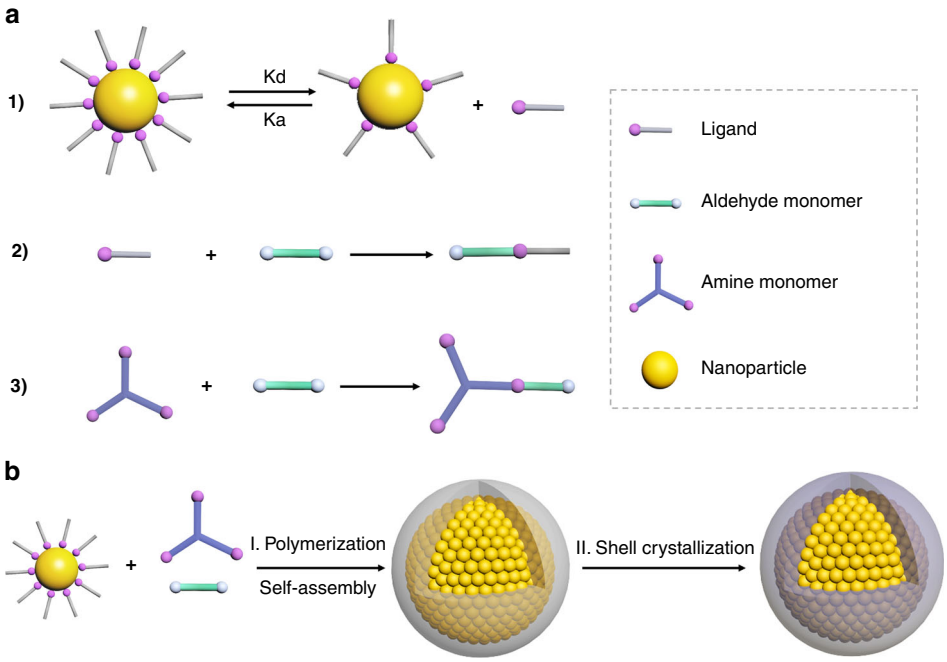

Fig. 1 Design concept for hybridization of nanoparticles with COF. **a** Chemical reactions within the system. (1) Schematic representation of dynamic adsorption/desorption equilibrium of ligands on nanoparticles. (2) Formation of dynamic covalent bond (imine bond) between two molecules bearing aldehyde and amine groups, respectively. (3) Formation of dynamic covalent bond between aldehyde and ligands for nanoparticle surface coating. **b** Synchronization of nanoparticle self-assembly and polymerization leads to the formation of core/shell structure, followed by the crystallization of shell materials into porous covalent organic frameworks

formation of TAPB–PDA polymer is initialized on the surface of the emulsion droplet, and the reaction is suppressed with the formation a polymer shell, which hampers the diffusion of monomer (TAPB or PDA) through polymer shell and produces hollow interior. We note that this rate control of the polymerization plays a pivotal role during the synthesis nanoparticles/COFs hybrids, which will be discussed later.

Small angle X-ray scattering (SAXS) measurement indicates that these colloidal particles are amorphous (denoted as Amor-TAPB–PDA) (Fig. 2m). The amorphous structure of Amor-TAPB–PDA is also confirmed by the calculation of the apparent Brunauer–Emmet–Teller (BET) area from N_2 sorption experiments performed at 77 K, showing a low BET surface area (Fig. 2n, $A_{BET} = 54.5\ m^2\ g^{-1}$).

Crystallization of Amor-TAPB–PDA colloidal particles takes place in the presence acetic acid at 70 °C (denoted as COF-TAPB–PDA), and the samples are analyzed by SEM, N_2 sorption, and SAXS. SEM images (Fig. 2e, f and Supplementary Fig. 6b, d) show that the size of the colloidal particles is retained after crystallization. However, a magnified image reveals that the surface of the particles is rougher compared to that of Amor-TAPB–PDA. SAXS of COF-TAPB–PDA displays two peaks at $q = 1.9$ and $3.6\ nm^{-1}$, corresponding to the (100) and (110) crystal planes of the particles. COF-TAPB–PDA exhibits reversible type IV isotherm, which is one of the main characteristics of mesoporous materials. The BET surface area of COF-TAPB–PDA is calculated to be $\sim 649\ m^2\ g^{-1}$, which is significantly improved compared to that of Amor-TAPB–PDA (see Supplementary Fig. 5).

This emulsion template synthesis of colloidal COFs can be also extended to other imine-based COF materials. When the amine and aldehyde organic subunits are replaced by tetrakis(4-aminophenyl)methane (TAPM) and bis(octyloxy)terephthalaldehyde (OTP), respectively, crystalline COF-TAPM–PDA and COF-TAPB–OTP colloidal particles can be successfully prepared (see Supplementary Figs. 8, 9 and 10).

Synchronization of nanoparticle self-assembly with imine bond formation in a drying droplet. The synthesis of nanoparticles/COFs hybrids is demonstrated initially with 4.5 nm Au nanoparticles capped with oleylamine (Au@OAM) (Supplementary Fig. 13a) and TAPB-PDA COFs. Au nanoparticles are synthesized according to the reported literature and their surfaces are capped with oleylamine (Fig. 3)[53]. In a typical experiment, TAPB and PDA are added to 1 mL of THF containing 1 mg of Au@OAM. The solution is well mixed by sonication at room temperature. Note that the surface plasmon resonance (SPR) band of the Au@OAM in THF does not shift after the addition of the TAPB and PDA, which indicates that these Au nanoparticles remain in isolation and do not aggregate (Supplementary Fig. 11). With the emulsification of 4 mL of 20 mg mL^{-1} DTAB solution and the 1 mL of THF solution, the organic subunits and the Au@OAM nanoparticles are evenly distributed within the emulsion droplets, and these Au@OAM nanoparticles tend to adsorb on the droplet interface, which is driven by the minimization of interfacial energy[47].

The polymerization of TAPB–PDA is triggered when the catalyst $Sc(OTf)_3$ is added into the emulsion[49,50]. After the addition of $Sc(OTf)_3$ at 15 °C for 2 min, the emulsion is heated to 70 °C and kept at this temperature for 30 min to evaporate the inner THF phase. The resulting Amor-TAPB–PDA–Au hybrids are washed twice with methanol and dispersed in deionized water to form stable colloids with a gray color (Fig. 3d). TEM images in Fig. 3a–c reveal that these particles have a core/shell morphology with a dark center and a pale periphery, indicating the formation of Au/(Amor-TAPB–PDA) core/shell structures. The average diameter, determined by counting more than 500 particles, is 275.8 nm. A magnified TEM image in Fig. 3c further shows that Au nanoparticles are self-assembled into three-dimensional superlattices. The core/shell structure is further confirmed by high annular dark field scanning TEM (HAADF-STEM) image and X-ray energy dispersive spectroscopy (STEM-EDS) (Fig. 3e).

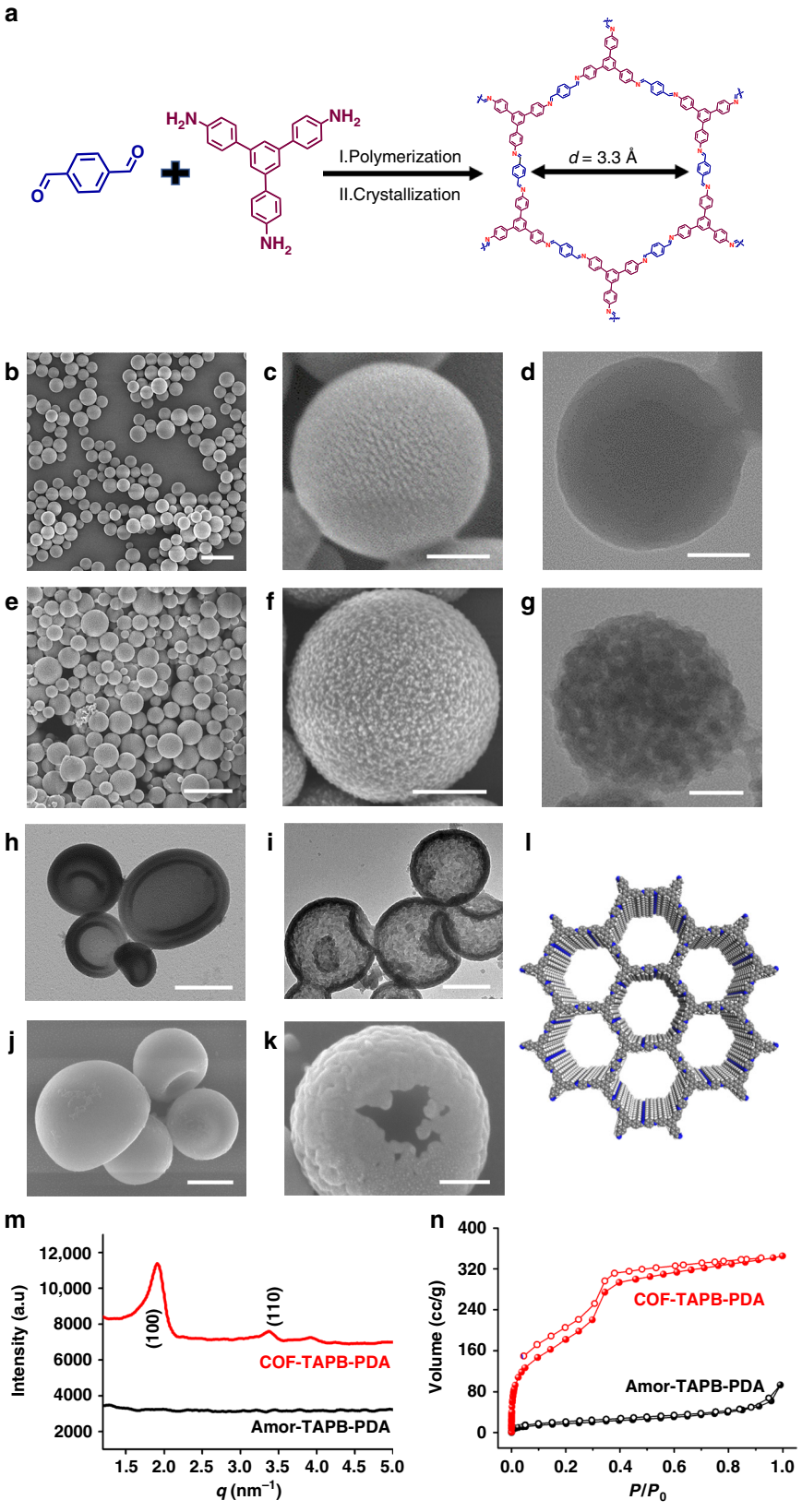

The nanoparticle ordering of the ensembles is further probed by SAXS, and two main peaks can be observed at $q = 0.18$ and 0.79 nm^{-1}, corresponding to face-centered-cubic (fcc) packing of the Au nanoparticles within the Amor-TAPB–PDA. In addition, the near field coupling effect within the Au nanoparticle assemblies is expected, which can be observed in the nontrivial red shift of the SPR band compared to the isolated Au nanoparticles (Fig. 3f). The above results clearly show that Au nanoparticle superlattices are successfully encapsulated in the Amor-TAPB–PDA. A similar mild annealing process as described

Fig. 2 Controlled polymerization by emulsion droplets. **a** Reaction scheme of COF-TAPB-PDA from 1,3,5-Tris(4-aminophenyl)benzene (TAPB) and P-phthalaldehyde (PDA). **b**, **c** SEM images of Amor-TAPB-PDA colloidal particles produced under the polymerization temperature of 70 °C; **d** TEM image of Amor-TAPB-PDA colloidal particles produced under the polymerization temperature of 70 °C; **e**, **f** SEM images and TEM image (**g**) of COF-TAPB-PDA spheres after crystallization process. **h**, **i** TEM images of Amor-TAPB-PDA (**h**) and COF-TAPB-PDA (**i**) hollow spheres, respectively. **j**, **k** SEM image of Amor-TAPB-PDA (**j**) and COF-TAPB-PDA (**k**) hollow spheres, respectively. **l** The schematic reprsentation of COF-TAPB-PDA. **m** One-dimensional SAXS profile of Amor-TAPB-PDA and COF-TAPB-PDA colloidal particles produced under the polymerization temperature of 70 °C. Curve of COF-TAPB-PDA shows the $d = 2\pi/q = 3.3$ nm at 1.9 nm^{-1}. **n** N_2 adsorption-desorption isotherms of Amor-TAPB-PDA and COF-TAPB-PDA produced under the polymerization temperature of 70 °C. The BET surface areas of the corresponding COF-TAPB-PDA and Amor-TAPB-PDA are calculated to be 649.0 and 54.5 m^2/g, respectively. Scale bar: **b**, **e**, **h**, **i**, **j** 500 nm; **c**, **d**, **f**, **k** 100 nm; **g** 50 nm

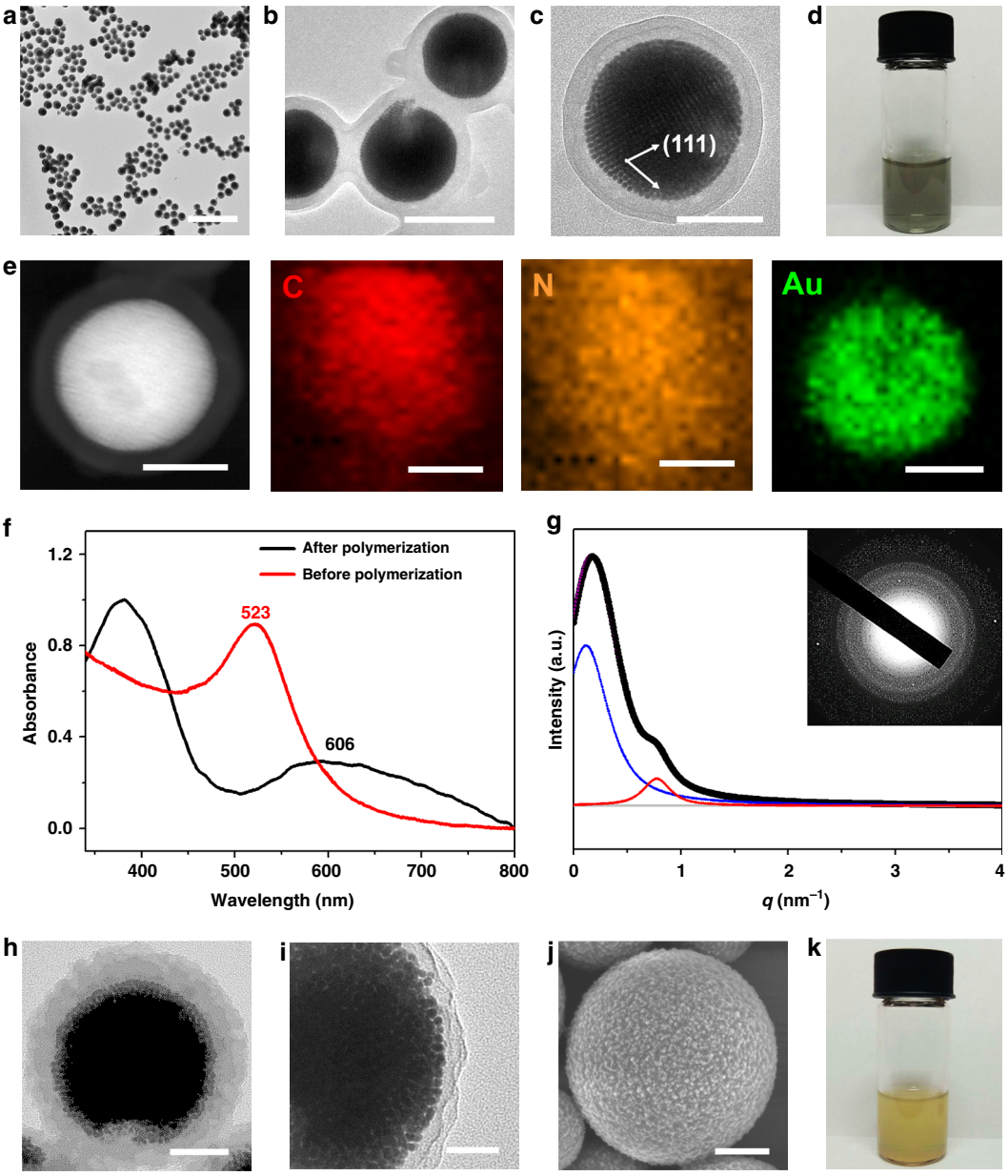

Fig. 3 Synchronization of nanoparticle self-assembly and TAPB-PDA polymerization. **a**–**c** TEM images of Au/(Amor-TAPB-PDA) core/shell hybrids under the polymerization temperature of 15 °C. **d** Optical image of suspension of Au/(Amor-TAPB-PDA) particles. **e** HAADF-STEM images and EDS-STEM of Au/(Amor-TAPB-PDA) core/shell structures. **f** UV-Vis spectra of a mixture of Au nanoparticles and TAPB-PDA monomers before and after polymerization. **g** One-dimensional SAXS file of Au/(Amor-TAPB-PDA) suspension. **h**, **i** TEM images of Au/(COF-TAPB-PDA); **j** SEM image of Au/(COF-TAPB-PDA); **k** optical image of suspension of Au/(COF-TAPB-PDA) particles. Scale bar: **a** 2 μm; **b** 200 nm; **c**, **e** 100 nm; **h**, **j** 50 nm; **i** 20 nm

above is carried out, resulting in phase transition of TAPB–PDA from amorphous to crystalline structure. After crystallization, both the core/shell morphology and the nanoparticle ordering retain, suggesting the formation of Au/(COF-TAPB–PDA) core/shell hybrids (Fig. 3h, i).

We emphasize that the amine-containing capping ligand on the nanoparticles is of particular importance to the interactions between nanoparticles and organic subunits (see Fig. 1). The amine capping ligands on nanoparticles undergo dynamic ligand adsorption/desorption on the nanoparticle surface when those nanoparticles are dispersed in a good solvent (Fig. 1a). Hence the bonding between nanoparticles and capping ligand can be described by its adsorption and desorption equilibrium constant, K, and the adsorption and desorption kinetic constants, k_a and k_d, respectively. The detached amine ligands can react with aldehyde in the nearest loci of the nanoparticles to form the imine bond, which is confirmed by the FTIR result from a control experiment in the presence of Au@OAM, PDA and $Sc(OTf)_3$ (Supplementary Fig. 12). This is nontrivial in the formation of Au/(Amor-TAPB–PDA) core/shell structures. In a control experiment, when Au nanoparticles are capped with dodecanethiol (Au@DDT), we cannot produce the Au/(Amor-TAPB–PDA) core/shell structures, instead is the exclusion of Au@DDT nanoparticles from Amor-TAPB–PDA (Supplementary Fig. 14). We note that the surface ligands of the nanoparticles are of particular importance to the integration of COF with nanoparticles. As reported previously[47], the emulsification can result in the adsorption of these hydrophobic nanoparticles on the droplet surface. This process is spontaneous and is driven by the sum of interfacial energy and the van der Waals interactions between the aliphatic chain of the surface ligands capped on nanoparticles and the hydrophobic tails of the surfactants (i.e. DTAB). Such nanoparticle monolayer adsorbed at the oil/water interface can significantly influence the interfacial polymerization because the catalyst in the water phase have limited access to the monomers (TAPB/PDA). When the surface ligands of the nanoparticles are amines, these amines can also react with PDA in the presence of catalyst (shown in Fig. 1). However, when the surface ligands of the nanoparticles are not amines, indicating that these nanoparticles are inertia layer during the interfacial polymerization process. As a consequence, these “inertia” nanoparticles (such as DDT-coated Au nanoparticles) are weakly attached to the surface of the polymer particles (shown in Supplementary Figs. 14b, c and 17b, c). These Au nanoparticles can be easily detached from TAPB–PDA polymer because the interaction between Au@DDT and TAPB–PDA polymer is the bond-free van der Waals interactions.

Hence this method can be generalized and can be applied to other nanoparticles capped with OAM either during or after synthesis, such as Pt@OAM, Pd@OAM, and Fe_3O_4 capped with mixed ligands of OAM and oleic acid (Fe_3O_4@OAM/OA) (Supplementary Figs. 15 and 16). Furthermore, the formation nanoparticles/COFs core/shell structure is also valid for other nonspherical nanoparticles, such as MnO nanocubes and Gd_2O_3 nanoplatelets (Supplementary Fig. 17). In addition, the formation core/shell structure is also valid for other materials, such as MOF (UiO-66) and SiO_2 (Supplementary Figs. 18 and 19).

Modulation of spatial distribution of nanoparticles within COFs. Next, we demonstrate that self-assembly of nanoparticles within COFs can be controlled by the temperature. As already described, the polymerization rate of TAPB–PDA is accelerated with the increase of temperature. We systematically tune the polymerization from 0 to 70 °C, while keeping other synthetic parameters constant. TEM images show that when the polymerization temperature is low (0, 15, and 20 °C), Au/(Amor-TAPB–PDA) core/shell structures can be produced with the formation of Au nanoparticle superlattices (Supplementary Fig. 20a–c). However, when the polymerization temperature is increased to 30 °C, the morphology of the particles drastically changes. TEM image in Fig. 4b, c shows that Au nanoparticles are sparsely distributed within the Amor-TAPB–PDA particles, instead of the close packing observed in a lower temperature (0, 15, and 20 °C). This result is also confirmed by HAADF-STEM and EDS-STEM characterization (Fig. 4f, g). EDS mapping reveals that C, N, and Au elements are all distributed homogeneously over the entire particles, indicating that Au nanoparticles are randomly trapped in the Amor-TAPB–PDA. When the polymerization is triggered at 50 or 70 °C, we find that Au/(Amor-TAPB–PDA) core/shell structures can be produced (Fig. 4i, j). Note that the shell thickness of the Amor-TAPB–PDA is nontrivially increased compared to that of a shell produced at 15 °C.

SERS properties of nanoparticles/COFs hybrids. The integration of Au nanoparticles and COF-TAPB–PDA into hybridized structures might generate many new functionalities. The fully encapsulated Au nanoparticles within COFs give a promising opportunity to exploit the SERS capabilities of the Au nanoparticles and their assemblies as embedded probes for detection of molecular species diffusing inside the COFs. Raman scattering of the molecules extremely close to surfaces of plasmonic materials is markedly enhanced, which is generally understood as the localized surface plasmon modes. This SERS signal can be further nontrivially enhanced by the interparticle plasmonic coupling enabled by the self-assembly of metal nanoparticles[54–56].

The SERS measurements of both Au/(Amor-TAPB–PDA) and Au/(COF-TAPB–PDA) samples obtained at different temperatures (15 and 30 °C) are carried out by using Rhodamine 6G (R6G) as a Raman probe molecule (Fig. 5). The Raman bands at 1165, 1561, 1589 cm^{-1} are originated from TAPB–PDA. The bands at 1311 cm^{-1} are the most intense assigned to R6G and selected as featured band to study Raman signal enhancement[57–59]. First of all, let us compare the peak intensities for Au/(Amor-TAPB–PDA) at 15 and 30 °C, which are denoted as Au30/(Amor-TAPB–PDA) and Au15/(Amor-TAPB–PDA), respectively. Figure 5c shows that Au15/(Amor-TAPB–PDA) has a much lower enhancement factor (EF) than that of Au30/(Amor-TAPB–PDA), which indicates that the access of R6G molecules to the surface of plasmonic Au nanoparticle is hampered for Au15/(Amor-TAPB–PDA). However, when the shell of TAPB–PDA crystallize into rigid porous structures (Au15/(COF-TAPB–PDA) and Au30/(COF-TAPB–PDA)), the results drastically change. The Au15/(COF-TAPB–PDA) has a ~20 fold increase in the peak intensity compared to that of Au15/(Amor-TAPB–PDA), which can be attributed to the gating effect from the porous structure. Note that there is no apparent increase in the peak intensity when comparing Au30/(Amor-TAPB–PDA) with Au30/(COF-TAPB–PDA). This indicates that the molecular diffusion here is not the key factor that determines the enhanced factor. The sparsely distributed Au nanoparticles underneath the TAPB–PDA shell can detect the probe molecules on the surface of TAPB–PDA shell. Besides, the peak intensity for Au15/(COF-TAPB–PDA) is much larger than that of Au30/(COF-TAPB–PDA), which can be understood by the interparticle plasmonic coupling enabled by the self-assembly of Au nanoparticles. Moreover, the self-assembled Au nanoparticles wrapped with COFs shows the sensitive detecting of R6G molecules at a low concentration of 10^{-7} M (Fig. 5d).

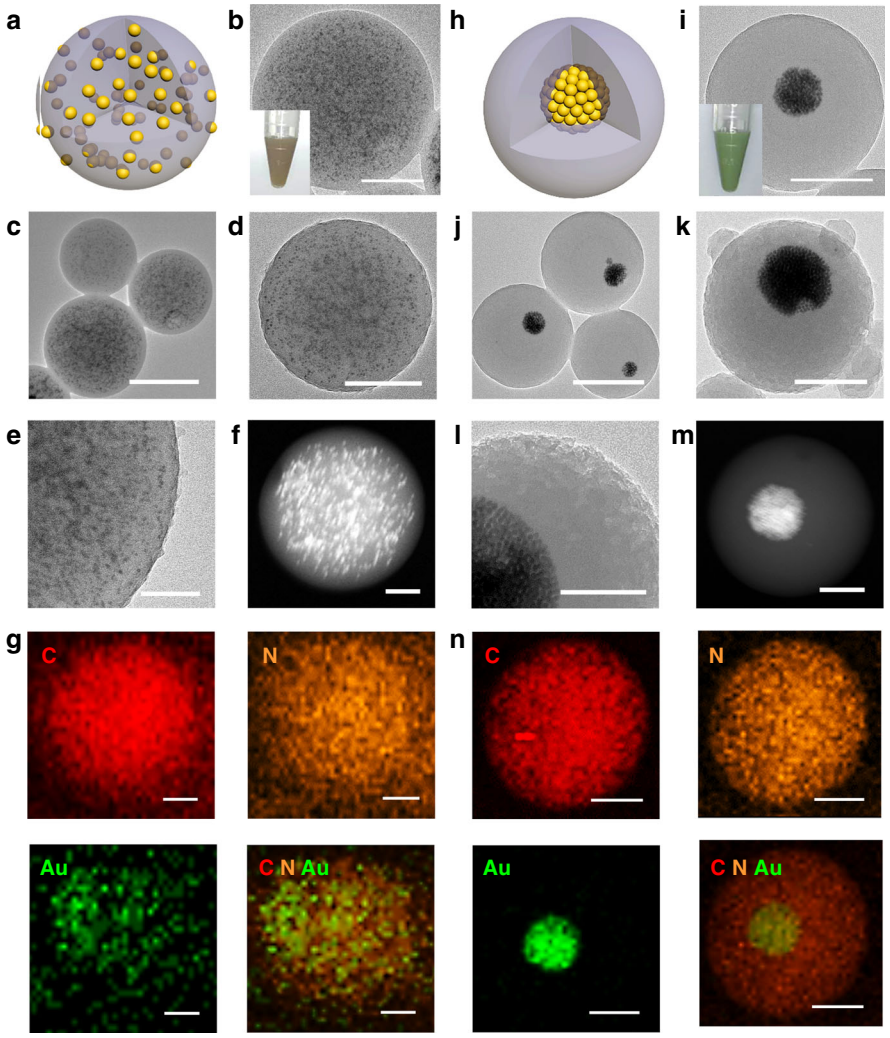

Fig. 4 Control over the spatial distribution of nanoparticles within COFs. **a**–**g** Assembly of Au nanoparticles in TAPB–PDA at 30 °C. **h**–**n** Assembly of Au nanoparticles in TAPB–PDA at 70 °C; **a**, **h** Cartoon illustration of hybrids of Au nanoparticles and TAPB–PDA polymer prepared at 30 °C (**a**) and 70 °C (**h**). TEM images of Au/(Amor-TAPB–PDA) hybrids prepared at 30 °C (**b**–**e**) and 70 °C (**i**–**l**). The insets are corresponding photographs in **b**, **i**; HAADF-STEM images and EDS-STEM of Au/(Amor-TAPB–PDA) sphere prepared at 30 °C (**f**, **g**) and 70 °C (**m**, **n**). Scale bar: **c** 300 nm; **b**, **i**, **d**, **j**, **k** 200 nm; **f**, **g**, **m**, **n** 100 nm; **e**, **l** 50 nm

Discussion

In summary, we have developed a simple, yet robust approach to encapsulate nanoparticles into COF colloids by using dynamic covalent reactions. The polymerization rate of organic subunits on the surface of emulsion droplets can be well controlled by adjusting the temperature. A lower temperature results in the formation of hollow structure, whereas a higher temperature leads to the formation of a dense structure. This feature couples the nanoparticle surface chemistry and imine-bond-based polymer. By controlling nanoparticle surface ligands that favorably interact with the organic subunits of polymers, nanoparticle–polymer interactions can be tailored. The dynamic adsorption/desorption of amine ligand on nanoparticle surface enables the construction of dynamic covalent bond between amine of the ligand and the aldehyde. In this manner, control over the spatial distribution of the nanoparticles within the COF colloids has been achieved. Therefore, the local environment and spatial arrangement of the nanoparticles can be tailored, opening further routes to engineer the collective physical properties of these hierarchically ordered nanoparticle assemblies. Another possible application of these nanoparticles/COF hybrid materials is in biomedicine. The porous structure of the shell can be used as reservoir to store bioactive molecules, and the Au nanoparticles can be responsive to the external stimuli, such as light. Plasmonic Au nanoparticles within the COF can generate photothermal effect upon the irradiation of light. Such photothermal effect can induce the increase of the temperature near the surface of Au nanoparticles. Hence the controlled release of these stored bioactive molecules can be realized when the specific interactions between the bioactive molecules and the COF is modulated.

Methods

Polymerization and crystallization of COF-TAPB–PDA. The COF-TAPB–PDA was prepared through a modified reaction. A solution of the monomers in THF was prepared according to the following procedure: TAPB (11 mg) and PDA (6 mg) were combined in a scintillation vial with 1 mL of THF and the resulting suspension was sonicated at room temperature until the monomers were fully dissolved. The aqueous solution of $Sc(OTf)_3$ (1 mM, 4 mL) containing 80 mg of DTAB was added to the above solution. The resulting emulsion was severely agitated by a vortex for 3 min. The emulsion was then heated to 70 °C and kept at this temperature for 30 min to evaporate the inner oil phase. The suspension was then allowed to cool to room temperature. The Amor-TAPB–PDA were washed twice with methanol. The Amor-TAPB–PDA (10 mg) was added to a bottle with dioxane/mesitylene solution (4:1 v/v, 2 mL). Distilled H_2O (0.43 mL) was added to

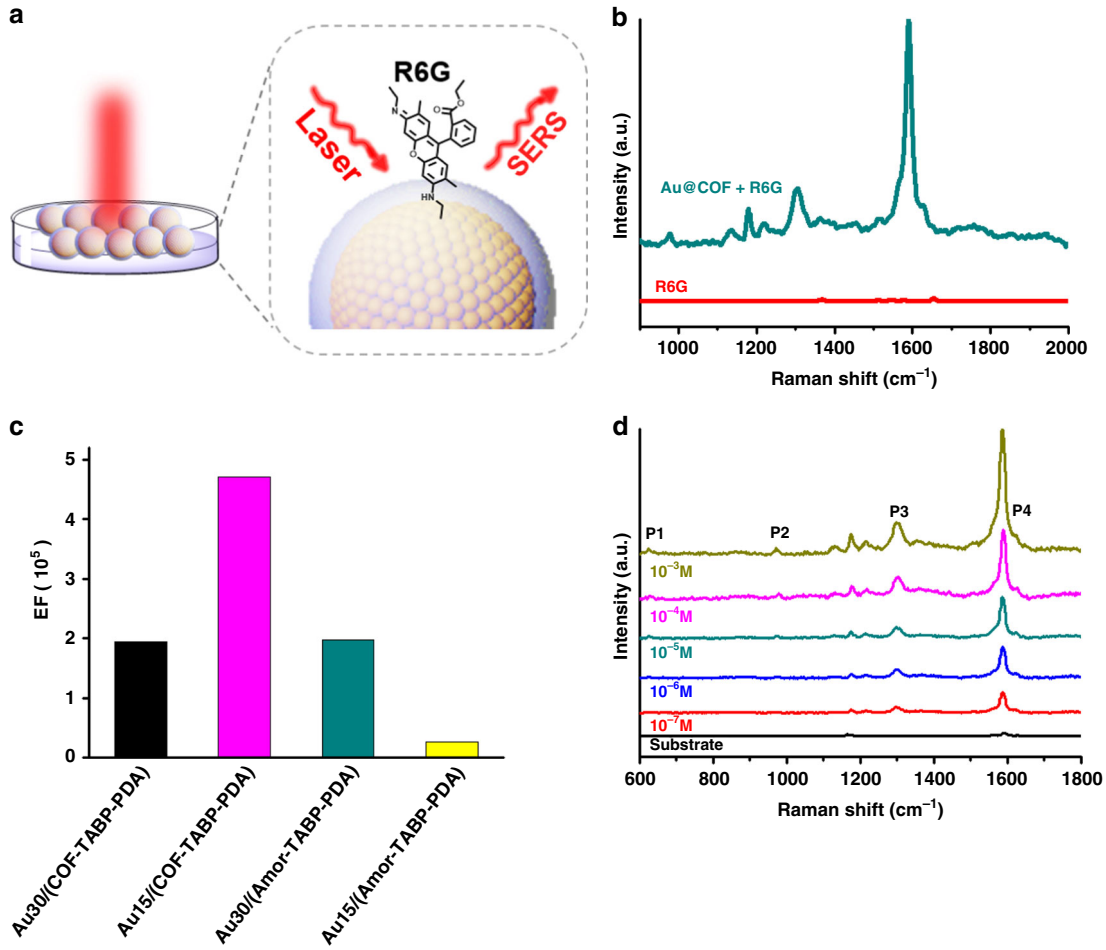

Fig. 5 SERS properties of the Au/(COF-TAPB-PDA) hybrids. **a** Cartoon illustration showing the SERS sensing of Au/(COF-TAPB-PDA) hybrids under laser excitation. Excitation wavelength: 473 nm. **b** Raman spectra of substrate Au/(COF-TAPB-PDA) prepared at 15 °C exposed to the 10^{-3} M Rhodamine 6G (R6G) and 10^{-3} M pure R6G. **c** EF of R6G (10^{-3} M) on the Au/COF prepared at 30 °C (black), Au/COF prepared at 15 °C (pink), Au/Amorphous prepared at 30 °C (green), and Au/Amorphous prepared at 15 °C (yellow) at 1311 cm^{-1}. **d** SERS spectra of R6G on Au/(COF-TAPB-PDA) prepared at 15 °C substrates at four different concentrations, 10^{-3}, 10^{-4}, 10^{-5}, 10^{-6}, and 10^{-7} M

the above solution, followed by CH_3CO_2H (0.63 mL). The resulting suspension was heated to 70 °C for 48 h. The COF-TAPB–PDA solid was isolated by centrifugation 5000 rpm, 2 min), rinsed with methanol, and subsequently dried under vacuum, yielding a yellow powder.

Polymerization and crystallization of COF-TAPB-OTP. A solution of the monomers in THF was prepared according to the following procedure: TAPB (11 mg) and OTP (17.4 mg) were combined in a scintillation vial with 1 mL of THF and the resulting suspension was sonicated at room temperature until the monomers were fully dissolved. The other steps are the same as the synthesis of COF-TAPB–PDA.

Polymerization and crystallization of COF-TAPM-PDA. A solution of the monomers in THF was prepared according to the following procedure: TAPM (8.9 mg) and PDA (6 mg) were combined in a scintillation vial with 1 mL of THF and the resulting suspension was sonicated at room temperature until the monomers were fully dissolved. The other steps are the same as the synthesis of COF-TAPB–PDA.

Assembly of Au@OAM/(COF-TAPB-PDA) microsphere. The 5.5 mg of TAPB, 3 mg of PDA, and 1 mg of Au@OAM were combined in a scintillation vial with 1 mL THF and the resulting suspension was sonicated at room temperature until the monomers were fully dissolved. 4 mL aqueous solution of DTAB (20 mg/mL) was added to the above solution and the resulting emulsion was severely agitated by a vortex for 3 min. The resulting suspension was stirred at specified temperature. Then, an aqueous solution of $Sc(OTf)_3$ (1 mM, 4 mL) was dropwise added into the resulting suspension slowly. Then, the emulsion was heated to 70 °C and kept at this temperature for 30 min to evaporate the inner oil phase. The suspension was then allowed to cool to room temperature. The resulting Au@OAM/(Amor-TAPB–PDA) was washed twice with methanol. The resulting suspension was added to a bottle with dioxane/mesitylene solution (4:1 v/v, 2 mL). Distilled H_2O (0.43 mL) and CH_3CO_2H (0.63 mL) was added to the solution. Then, the resulting suspension was heated to 70 °C for 48 h. The Au@OAM/(COF-TAPB–PDA) solid was isolated by centrifugation (8000 rpm, 3 min), rinsed with methanol, and subsequently dried under vacuum, yielding a green powder.

Synthesis of Au@OAM nanoparticle. The Au@OAM was prepared through a modified reaction. In a typical synthesis of Au@OAM, an orange precursor solution of toluene (10 mL), oleylamine (10 mL), and $HAuCl_4{\cdot}3H_2O$ (0.1 g) was prepared in air at room temperature and magnetically stirred under N_2 flow for 10 min. A solution containing 0.5 mmol of TBAB (0.0435 g), toluene (1 mL), and oleylamine (1 mL) was mixed by sonication and injected into the precursor solution. The reduction was instantaneously initiated and the solution changed to a deep purple color within 5 s. The mixture was allowed to react at 35 °C for 1 h before acetone (60 mL) was added to precipitate the Au@OAM. The production was collected by centrifugation (8000 rpm, 3 min), washed with acetone and redispersed in chloroform.

Data availability

The data that support the findings of this study are available from the corresponding author upon request.

Received: 18 June 2019; Accepted: 23 September 2019;
Published online: 25 October 2019

References

1. Lehn, J.-M. Toward complex matter: supramolecular chemistry and self-organization. *Proc. Natl Acad. Sci. USA* **99**, 4763–4768 (2002).
2. Balazs, A. C., Emrick, T. & Russell, T. P. Nanoparticle polymer composites: where two small worlds meet. *Science* **314**, 1107–1110 (2006).
3. Zhao, Y. et al. Small-molecule-directed nanoparticle assembly towards stimuli-responsive nanocomposites. *Nat. Mater.* **8**, 979–985 (2009).
4. Hollamby, M. J. et al. Directed assembly of optoelectronically active alkyl–π-conjugated molecules by adding n-alkanes or π-conjugated species. *Nat. Chem.* **6**, 690–696 (2014).
5. Webber, M. J., Appel, E. A., Meijer, E. W. & Langer, R. Supramolecular biomaterials. *Nat. Mater.* **15**, 13–26 (2015).
6. Bishop, K. J. M., Wilmer, C. E., Siowling Soh, S. & Grzybowski, B. A. Nanoscale forces and their uses in self-assembly. *Small* **5**, 1600–1630 (2009).
7. Whitesides, G. M. & Grzybowski, B. A. Self-assembly at all scales. *Science* **295**, 2418–2421 (2002).
8. Jones, M. R., Seeman, N. C. & Mirkin, C. A. Programmable materials and the nature of the DNA bond. *Science* **347**, 1260901 (2015).
9. Bai, Y., Luo, Q. & Liu, J. Protein self-assembly via supramolecular strategies. *Chem. Soc. Rev.* **45**, 2756–2767 (2016).
10. Collier, C. P., Vossmeyer, T. & Heath, J. R. Nanocrystal superlattices. *Annu. Rev. Phys. Chem.* **49**, 371–404 (1998).
11. Singh, G. et al. Self-assembly of magnetite nanocubes into helical superstructures. *Science* **345**, 1149–1153 (2014).
12. Jana., S., Davidson, P. & Abécassis, B. CdSe nanoplatelets: living polymers. *Angew. Chem. Int. Ed.* **128**, 9517–9520 (2016).
13. Groschel, A. H. et al. Guided hierarchical co-assembly of soft patchy nanoparticles. *Nature* **503**, 247–251 (2013).
14. Gao, C. et al. A user-friendly herbicide derived from photo-responsive supramolecular vesicles. *Nat. Commun.* **9**, 2967 (2018).
15. Guo, R., Liu, Z., Xie, X. M. & Yan, L. T. Harnessing dynamic covalent bonds in patchy nanoparticles: creating shape-shifting building blocks for rational and responsive self-assembly. *J. Phys. Chem. Lett.* **4**, 1221–1226 (2013).
16. Cote, A. P. et al. Porous, crystalline, covalent organic frameworks. *Science* **310**, 1166–1170 (2005).
17. Côté, A. P., El-Kaderi, H. M., Furukawa, H., Hunt, J. R. & Yaghi, O. M. Reticular synthesis of microporous and mesoporous 2D covalent organic frameworks. *J. Am. Chem. Soc.* **129**, 12914–12915 (2007).
18. Colson, J. W. & Dichtel, W. R. Rationally synthesized two-dimensional polymers. *Nat. Chem.* **5**, 453–465 (2013).
19. Ding, S. Y. & Wang, W. Covalent organic frameworks (COFs): from design to applications. *Chem. Soc. Rev.* **42**, 548–568 (2013).
20. Kandambeth, S., Venkatesh, V. & Shinde, D. B. Self-templated chemically stable hollow spherical covalent organic framework. *Nat. Commun.* **6**, 6786 (2015).
21. Dai, W. et al. Synthesis of a two-dimensional covalent organic monolayer through dynamic imine chemistry at the air/water interface. *Angew. Chem. Int. Ed.* **55**, 213–217 (2016).
22. Evans, A. M. et al. Seeded growth of single-crystal two-dimensional covalent organic frameworks. *Science* **361**, 52–57 (2018).
23. Hao, Q. et al. Confined synthesis of two-dimensional covalent organic framework thin films within superspreading water layer. *J. Am. Chem. Soc.* **140**, 12152–12158 (2018).
24. Das, G., Balaji Shinde, D., Kandambeth, S., Biswal, B. P. & Banerjee, R. Mechanosynthesis of imine, b-ketoenamine, and hydrogen-bonded imine-linked covalent organic frameworks using liquid-assisted grinding. *ChemComm* **50**, 1359–7345 (2014).
25. Han, S. S., Furukawa, H., Yaghi, O. M. & Goddard, W. A. III Covalent organic frameworks as exceptional hydrogen storage materials. *J. Am. Chem. Soc.* **130**, 11580–11581 (2008).
26. Doonan, C. J., Tranchemontagne, D. J., Glover, T. G., Hunt, J. R. & Yaghi, O. M. Exceptional ammonia uptake by a covalent organic framework. *Nat. Chem.* **2**, 235–238 (2010).
27. Xu, H., Gao, J. & Jiang, D. Stable, crystalline, porous, covalent organic frameworks as a platform for chiral organocatalysts. *Nat. Chem.* **7**, 905–912 (2015).
28. Liu, G., Sheng, J. & Zhao, Y. Chiral covalent organic frameworks for asymmetric catalysis and chiral separation. *Sci. China Chem.* **60**, 1015–1022 (2017).
29. Sun, Q. et al. Reaction environment modification in covalent organic frameworks for catalytic performance enhancement. *Angew. Chem. Int. Ed.* **58**, 8670–8675 (2019).
30. Xie, J. et al. Efficient visible light-driven water oxidation and proton reduction by an ordered covalent triazine-based framework. *Energy Environ. Sci.* **11**, 1617–1624 (2018).
31. Chandra, S. et al. Molecular level control of the capacitance of two-dimensional covalent organic frameworks: role of hydrogen bonding in energy storage materials. *Chem. Mater.* **29**, 2074–2080 (2017).
32. Thote, J. et al. A covalent organic framework-cadmium sulfide hybrid as a prototype photocatalyst for visible-light-driven hydrogen production. *Chem. Eur. J.* **20**, 15961–15965 (2014).
33. Biswal, B. P., Shinde, D. B., Pillai, V. K. & Banerjee, R. Stabilization of graphene quantum dots (GQDs) by encapsulation inside zeolitic imidazolate framework nanocrystals for photoluminescence tuning. *Nanoscale* **5**, 10556–10561 (2013).
34. Huang, N., Ding, X., Kim, J., Ihee, H. & Jiang, D. A photoresponsive smart covalent organic framework. *Angew. Chem. Int. Ed.* **54**, 8704–8707 (2015).
35. Lin, S. et al. Covalent organic frameworks comprising cobalt porphyrins for catalytic CO_2 reduction in water. *Science* **349**, 1208–1213 (2015).
36. Jin, E. et al. Designed synthesis of stable light-emitting two-dimensional sp(2) carbon-conjugated covalent organic frameworks. *Nat. Commun.* **9**, 4143 (2018).
37. Peng, P. et al. In situ charge exfoliated soluble covalent organic framework directly used for Zn–air flow battery. *ACS Nano* **13**, 878–884 (2019).
38. Yang, S. et al. 2D covalent organic frameworks as intrinsic photocatalysts for visible light-driven CO_2 reduction. *J. Am. Chem. Soc.* **140**, 14614–14618 (2018).
39. Ding, S. Y. et al. Construction of covalent organic framework for catalysis: Pd/COF-LZU1 in Suzuki–Miyaura coupling reaction. *J. Am. Chem. Soc.* **133**, 19816–19822 (2011).
40. Peng, Y. et al. Hybridization of MOFs and COFs: a new strategy for construction of MOF@COF core–shell hybrid materials. *Adv. Mater.* **30**, 1705454 (2018).
41. Zhang, F. M. et al. Rational design of MOF/COF hybrid materials for photocatalytic H_2 evolution in the presence of sacrificial electron donors. *Angew. Chem. Int. Ed.* **130**, 12282–12286 (2018).
42. Sun, Q., Aguila, B., Perman, J., Nguyen, N. & Ma, S. Flexibility matters: cooperative active sites in covalent organic framework and threaded ionic polymer. *J. Am. Chem. Soc.* **138**, 15790–15796 (2016).
43. Shi, X. et al. Imparting catalytic activity to a covalent organic framework material by nanoparticle encapsulation. *Appl. Mater. Int.* **9**, 7481–7488 (2017).
44. Tan, J., Namuangruk, S., Kong, W., Kungwan, N. & Wang, C. Manipulation of amorphous-to-crystalline transformation: towards the construction of covalent organic framework hybrid microspheres with NIR photothermal conversion ability. *Angew. Chem. Int. Ed.* **55**, 13979–13984 (2016).
45. Dong, A., Chen, J., Vora, P. M., Kikkawa, J. M. & Murray, C. B. Binary nanocrystal superlattice membranes self-assembled at the liquid–air interface. *Nature* **466**, 474–477 (2010).
46. Boles, M. A., Engel, M. & Talapin, D. V. Self-assembly of colloidal nanocrystals: from intricate structures to functional materials. *Chem. Rev.* **116**, 11220–11289 (2016).
47. Yang, Z. et al. Supracrystalline colloidal eggs: epitaxial growth and freestanding three-dimensional supracrystals in nanoscaled colloidosomes. *J. Am. Chem. Soc.* **138**, 3493–3500 (2016).
48. Nagaoka, Y. et al. Superstructures generated from truncated tetrahedral quantum dots. *Nature* **561**, 378–382 (2018).
49. Matsumoto, M. et al. Rapid, Low temperature formation of imine-linked covalent organic frameworks catalyzed by metal triflates. *J. Am. Chem. Soc.* **139**, 4999–5002 (2017).
50. Matsumoto, M. et al. Lewis-acid-catalyzed interfacial polymerization of covalent organic framework films. *Chem* **4**, 308–317 (2018).
51. Li, L., Li, L., Cui, C., Fan, H. & Wang, R. Heteroatom-doped carbon spheres from hierarchical hollow covalent organic framework precursors for metal-free catalysis. *Chem. Sus. Chem.* **10**, 4921–4926 (2017).
52. Pachfule, P., Kandmabeth, S., Mallick, A. & Banerjee, R. Hollow tubular porous covalent organic framework (COF) nanostructures. *ChemComm* **51**, 11717–11720 (2015).
53. Peng, S. et al. A facile synthesis of monodisperse Au nanoparticles and their catalysis of CO oxidation. *Nano Res.* **1**, 229–234 (2008).
54. Fleischmann, M., Hendra, P. J. & Mcquillan, A. J. Raman spectra of pyridine adsorbed at a silver electrode. *J. Chem. Phys. Lett.* **26**, 163–166 (1974).
55. Jeanmaire, D. L., Duyne, R. P. V., Jeanmaire, D. L. & Duyne, R. P. V. Surface raman spectroelectrochemistry: Part I. Heterocyclic, aromatic, and aliphatic amines adsorbed on the anodized silver electrode. *J. Electroanal. Chem.* **84**, 1–20 (1977).
56. Cong, S. et al. Noble metal-comparable SERS enhancement from semiconducting metal oxides by making oxygen vacancies. *Nat. Commun.* **6**, 7800 (2015).
57. Qiao, X., Su, B., Liu, C., Song, Q. & Wang, T. Selective surface enhanced raman scattering for quantitative detection of lung cancer biomarkers in superparticle@MOF structure. *Adv. Mater.* **30**, 1702275 (2017).
58. Sun, H. et al. Metal-organic frameworks as SERS substrates with high tailorability. *J. Am. Chem. Soc.* **141**, 870–878 (2019).
59. Osterrieth, J. W. M. et al. Core–shell gold nanorod@zirconium-based metal-organic framework composites as in situ size-selective raman probes. *J. Am. Chem. Soc.* **141**, 3893–3900 (2019).

Acknowledgements
This work was financially supported by the National Natural Science Foundation of China (Grant No. 21703120) and 1000 Young Talents Program. Z.Y. thanks Taishan Scholars Program of Shandong Province (tsqn201812011).

Author contributions
Z.Y. and J.W. conceived the idea and providing the guidance. .F.Z. performed the most of the experiments. F.Z., K.Z., and M.H. performed the nanoparticle synthesis. F.Z. and J.H. provided theoretical analysis. Y.Y. provided fruitful discussion. Z.Y. and J.W. wrote the manuscript with input from all authors.

Competing interests
The authors declare no competing interests.

Additional information
Supplementary information is available for this paper at https://doi.org/10.1038/s42004-019-0222-4.

Correspondence and requests for materials should be addressed to Z.Y., Y.Y. or J.W.

Reprints and permission information is available at http://www.nature.com/reprints

Publisher's note Springer Nature remains neutral with regard to jurisdictional claims in published maps and institutional affiliations.